Biogeochemistry (2023) 164:319–333
https://doi.org/10.1007/s10533-023-01054-7

BIOGEOCHEMISTRY LETTERS

Quantifying erosion rates and weathering pathways that maximize soil organic carbon storage

Joshua J. Roering · Brooke D. Hunter · Ken L. Ferrier · Oliver A. Chadwick · Kyungsoo Yoo · Adrian A. Wackett · Peter C. Almond · Lucas Silva · A. Mark Jellinek

Received: 11 February 2023 / Accepted: 22 May 2023 / Published online: 22 June 2023

Abstract Primary minerals that enter soils through bedrock weathering and atmospheric deposition can generate poorly crystalline minerals (PCM) that preferentially associate with soil organic carbon (SOC). These associations hinder microbial decomposition and the release of CO_2 from soils to the atmosphere, making them a critical geochemical control on terrestrial carbon abundance and persistence. Studies that explore these relationships are typically derived from soil chronosequences that experience negligible erosion and thus do not readily translate to eroding landscapes. Here, we propose a theoretical framework to estimate steady-state PCM density and stocks for hilly and mountainous settings by coupling geochemical and geomorphic mass balance equations that account for soil production from bedrock and dust, soil erosion, PCM formation from weathering, and the transformation of PCMs into crystalline phases. We calculate an optimal erosion rate for maximum PCM abundance that arises because PCMs are limited by insufficient weathering at faster erosion rates and loss

Responsible Editor: Stephen D. Sebestyen.

Supplementary Information The online version contains supplementary material available at https://doi.org/10.1007/s10533-023-01054-7.

J. J. Roering (✉) · B. D. Hunter
Department of Earth Sciences, University of Oregon, Eugene, OR 97403-1272, USA
e-mail: jroering@uoregon.edu

K. L. Ferrier
Department of Geoscience, University of Wisconsin-Madison, Madison, WI 53706, USA

O. A. Chadwick
Department of Geography, University of California, Santa Barbara, Santa Barbara, CA 93106-4060, USA

K. Yoo
Department of Soil, Water, and Climate, University of Minnesota, St Paul, MN 55108, USA

A. A. Wackett
Department of Ecology and Environmental Sciences, Umeå University, 907 36 Umeå, Västerbotten, Sweden

A. A. Wackett
Department of Earth and Planetary Sciences, Stanford University, Stanford, CA 94305-2210, USA

P. C. Almond
Department of Soil and Physical Sciences, Lincoln University, Lincoln 7647, Canterbury, New Zealand

L. Silva
Environmental Studies Program and Institute of Ecology and Evolution, University of Oregon, Eugene, OR 97405-1272, USA

A. M. Jellinek
Department of Earth, Ocean and Atmospheric Sciences, University of British Columbia, Vancouver, BC V6T 1Z4, Canada

via "ripening" into more crystalline forms at slower erosion rates. The optimal erosion rate for modeled hilltop soil is modulated by reaction rate constants that govern the efficiency of primary mineral weathering and PCM ripening. By comparing our analysis with global compilations of erosion and soil production rates derived from cosmogenic nuclides, we show that landscapes with slow-to-moderate erosion rates may be optimal for harboring abundant PCM stocks that can facilitate SOC sequestration and limit turnover. Given the growing array of erosion-topography metrics and the widespread availability of high-resolution topographic data, our framework demonstrates how weathering and critical zone processes can be coupled to inform landscape prioritization for persistent SOC storage potential across a broad range of spatial and temporal scales.

Keywords Weathering · Soil organic carbon · Poorly crystalline minerals · Erosion rate · Soil residence time · Soil organic matter · Geomorphology · Hillslope · Regolith

Introduction

The pedosphere contains more carbon than the atmosphere and biosphere combined (Jobbágy and Jackson 2000). Thus, changes in global soil organic carbon (SOC) stocks can have substantial impacts on atmospheric CO_2, implying that land management strategies for optimizing SOC storage may be an important tool for addressing climate change (Georgiou et al. 2021). Determining the extent to which soils can serve as an effective venue for carbon storage depends on the pace of SOC turnover and SOC persistence (Lavallee et al. 2020). With the key exception of deep organic soils subject to saturation and anoxic conditions (e.g., peatlands), the persistence of SOC is largely determined by the coupling of dissolved and/or microbially-processed organic matter with reactive mineral surfaces to generate relatively long-lived mineral-associated organic carbon (MOC) forms (e.g., Doetterl et al. 2015; Grant et al. 2022). These stabilizing associations with minerals can limit microbial access to SOC, thereby promoting SOC accumulation and persistence. In turn, a multitude of biogeochemical studies have sought to analyze how soil texture and mineralogy modulate the density and net inventory of SOC and MOC in soils (Georgiou et al. 2022; Kramer and Chadwick 2018; Schmidt et al. 2011; Torn et al. 1997). Despite the complex and dynamic nature of organo-mineral interactions (Kleber et al. 2021), studies from a diverse array of settings (as determined by landform age, parent material, and climate) demonstrate a strong correlation between poorly crystalline minerals (PCM) composed of Al and Fe hydroxides (e.g., ferrihydrite, allophane, and imogolite) and SOC (e.g., von Fromm et al. 2021). This association between PCM production and SOC retention is commonly attributed to the high degree of hydration, extensive surface area, and variable charge of PCMs (Chorover et al. 2004), although recent studies also explore the degree to which SOC decomposition drives PCM concentrations (Hall and Thompson 2022). Regardless, carbon dating suggests that MOC turnover rates are substantially slower than those measured for particulate organic carbon, demonstrating the strength of soil mineral controls on SOC persistence and their importance for informing SOC sequestration strategies (Lehmann and Kleber 2015).

In natural landscapes, PCMs originate from the weathering of primary minerals sourced from underlying bedrock (or other substrates) as well as atmospheric deposition (e.g., dust). Weathering rates and pathways are commonly studied using soil chronosequences from dated fluvial, marine, glacial, or volcanic surfaces subject to negligible surface erosion (Lawrence et al. 2015; Masiello et al. 2004; Torn et al. 1997). These studies demonstrate strong linkages between secondary minerals and SOC stocks, including age-dependent trends in mineral reactivity on microbial composition, soil respiration, and SOC stabilization (Doetterl et al. 2018). In particular, seminal work by Torn et al. (1997) in Hawaii shows that SOC fractions and stocks, PCMs, and ^{14}C ages increase for basalt flows with ages spanning 10^2 to 10^5 years old before decreasing as flow ages approach 10^6 years. The ~ 10^5-ya peak in PCMs, SOC, and ^{14}C ages occurs because the older surfaces are subject to progressive "ripening" or dehydration of PCMs to crystalline clay phases and oxides, such as gibbsite, goethite, and kaolinite, which have comparably low surface area and charge densities relative to PCMs. This ripening results in a decreased affinity for SOC stabilization. This soil age "sweet spot" for SOC storage has also been observed in other chronosequence studies, although the peak age associated with maximum SOC and PCM density appears to vary, likely

reflecting differences in climate, parent materials, and/or SOC dynamics (Garcia Arredondo et al. 2019; Hunter et al. in press; Lawrence et al. 2015).

Because the vast majority of the Earth surface is subject to erosion, applying PCM-SOC relationships derived from chronosequence datasets requires consideration of both landscape age and erosional history (Slessarev et al. 2019). The geomorphic community has leveraged a vast array of tools, including stream network analysis, hillslope morphometrics, and erosion rates calibrated with cosmogenic nuclides, to show that variability in long-term erosion rates are substantial and pervasive across most hilly and mountainous landscapes (Mudd 2017). As a result, systematic variations in weathering, PCMs, and MOC stocks are likely, but the impact of these variations has not been incorporated into commonly used SOC inventory databases like SoilGrids (Poggio et al. 2021). Studies that bridge soil science and geomorphology often use the soil particle residence time framework, defined as the average length of time that soil particles spend in a soil of thickness, H, between entry (via bedrock-soil conversion) and exit (via erosion, E). This metric serves as a characteristic timescale during which biogeochemical processes occur on actively eroding hillslopes before soils are exported to fluvial networks or depositional zones (Almond et al. 2007; Mudd and Yoo 2010). With one notable exception (Wang et al. 2018), studies that quantify soil mineralogy and organic matter on hillslopes that occupy an erosional gradient are limited. As a result, we lack a generalized theoretical framework to characterize PCM abundance across erosional settings.

Here, we propose a predictive model for PCM concentrations and stocks in soil-mantled, erosional settings by coupling a geomorphic soil production function with a geochemical mass balance for the inputs and losses of primary minerals and PCMs. Our approach takes inspiration from recent work (Slessarev et al. 2022) by accounting for the weathering of primary minerals to PCMs but also incorporates the subsequent ripening of PCMs into less reactive crystalline phases. We demonstrate that the soil age sweet spot of maximum PCM abundance observed in chronosequence studies has an analogy in erosional settings, which corresponds to the erosion rate associated with maximum PCM concentration and stocks that promote MOC formation. This theoretical framework should inform the scaling of global and regional SOC databases and facilitate carbon-based land management decision-making across the erosional landscapes that constitute the vast majority of the Earth surface.

Methods

Overview

To calculate how erosion rate modulates the concentration and inventory of PCMs that promote SOC persistence, we modified a mass balance weathering model for ridge crest soils on eroding hillslopes (Ferrier and Kirchner 2008), hereafter referred to as FK08. This model tracks the input and fate of a suite of minerals in a well-mixed, eroding soil, which allows us to test erosion rate controls on soil geochemistry. In our modification depicted in Fig. 1, soils gain mass by the conversion of bedrock (or underlying substrate) and dust incorporation, they lose mass via physical erosion and chemical dissolution, and their composition changes according to the transformation of mineral phases into secondary phases. Our modification enables the model to generate secondary minerals, such as PCMs and clays, at a rate that depends directly on the weathering rate of primary mineral phases (such as plagioclase feldspar). In FK08, by contrast, secondary mineral generation was modeled as a constant value, independent of primary mineral weathering rates.

Theory: soil mineralogy and weathering pathways on eroding hillslopes

We expand the theoretical framework of FK08 to incorporate mineral supply from dust incorporation as well as secondary mineral generation and solute production as independent reactions for any given mineral phase. Most generally, the revised theory accounts for the rate of change of mass for mineral phase X in soil according to the balance of inputs and losses of X:

$$\frac{d\left(\rho_s H C_{Xs}\right)}{dt} = \sum Input_X - \sum Loss_X \quad (1)$$

where ρ_s is soil density (M L^{-3}), H is soil thickness (L), and C_{Xs} is concentration of mineral phase X in soil. Here, we account for inputs of X (M L^{-2} T^{-1}) arising from soil production (i.e., the conversion

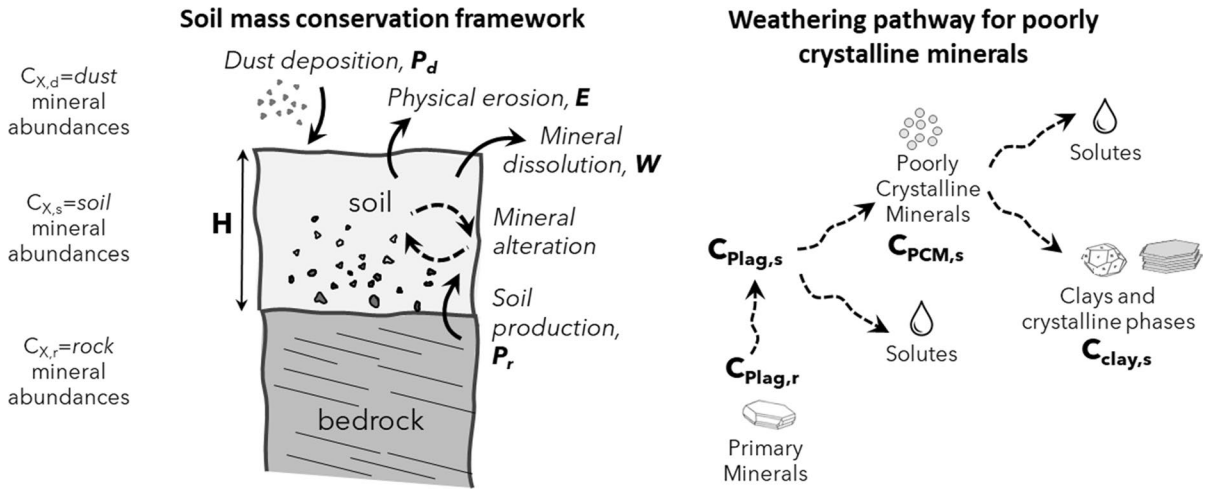

Fig. 1 **A** Schematic of soil-mantled profile subject to mass loss via physical erosion and mineral dissolution, mass gain via dust deposition and soil production, and mineral transformation via secondary mineral generation. **B** The weathering pathways and mass balance described by our model represent the input of primary minerals from bedrock into soil followed by the weathering of those minerals into poorly crystalline minerals (or PCMs), which are highly effective at sorbing soil organic carbon (SOC). These PCMs can then subsequently ripen into clays and crystalline pedogenic mineral phases that are less conducive to organic associations

of bedrock or substrate to mobile soil), dust deposition, and alteration of other mineral phases to X, as follows:

$$\textit{Input rate of X from underlying rock or substrate} = P_r C_{Xr} \tag{2a}$$

$$\textit{Input rate of X from atmospheric or dust deposition} = P_d C_{Xd} \tag{2b}$$

$$\textit{Input rate of X from alteration of other mineral phases} = \sum_{j=1}^{n} \rho_s H C_{js} K_{j,X} \tag{2c}$$

In addition, we account for losses (M L^{-2} T^{-1}) of mineral phase X owing to physical erosion, dissolution, and alteration of X to other mineral phases, according to:

$$\textit{Loss rate of X to physical erosion} = EC_{Xs} \tag{3a}$$

$$\textit{Loss rate of X to solutes} = \rho_s H C_{Xs} K_{X,sol} \tag{3b}$$

$$\textit{Loss rate of X by alteration to other mineral phases} = \sum_{j=1}^{n} \rho_s H C_{Xs} K_{X,j} \tag{3c}$$

where P_r and P_d are soil and dust production rate (M L^{-2} T^{-1}), respectively, E is physical erosion rate (M L^{-2} T^{-1}), C_{Xr} and C_{Xd} are concentrations of mineral phase X in rock and dust (M M^{-1}), respectively, and $K_{X,j}$ is an effective weathering rate constant for the conversion of parent mineral phase X to daughter mineral phase or product j (T^{-1}), where X and j can either serve as parent or daughter phases and solute can only serve as a daughter product. Here, daughter phases are pedogenic minerals, such as PCMs (e.g., allophane) or more intensively weathered clays (e.g., kaolinite). The $K_{X,j}$ term is a bulk weathering parameter that combines the dissolution (or reaction) rate constant and specific surface area terms that are often used to model chemical weathering (Ferrier and West 2017).

Assuming constant soil density, we calculate the rate of change of soil thickness (H) by accounting for inputs of soil production and dust and losses to physical erosion and solutes:

$$\frac{dH}{dt} = \frac{1}{\rho_s}\left(P_0 e^{-\alpha H} + P_d - E - \rho_s H \sum_{j=1}^{n} C_{js} K_{j,sol}\right) \quad (4)$$

where P_0 is the peak or maximum soil production rate (M L^{-2} T^{-1}) and α is a scaling parameter (L^{-1}) associated with an empirical soil production relationship supported by abundant field evidence (Heimsath et al. 2012), which indicates that soil production rates decline exponentially with depth:

$$P_r = P_0 e^{-\alpha H} \quad (5)$$

By applying the product rule for differentiation of Eq. 1 and combining Eqs. 1 to 5, we obtain an expression for the rate of change of the concentration of mineral phase X in soil:

$$\begin{aligned}\frac{dC_{Xs}}{dt} =& \frac{P_0 e^{-\alpha H}}{\rho_s H}\left(C_{Xr} - C_{Xs}\right) + \frac{P_d}{\rho_s H}\left(C_{Xd} - C_{Xs}\right) \\ &+ \sum_{j=1}^{n} C_{js} K_{j,X} - C_{Xs} K_{X,sol} - C_{Xs} \sum_{j=1}^{n} K_{X,j} \\ &+ C_{Xs} \sum_{j=1}^{n} C_{js} K_{j,sol}\end{aligned} \quad (6)$$

Taken together, Eqs. 4 and 6 can be used to calculate how the mineral composition of hillslope soils evolves with time and is subject to model assumptions, including negligible chemical alteration of underlying substrate that enters the soil column (e.g., bedrock weathering) and minimal soil transport from upslope locations, such that the model is primarily relevant for ridgecrest or hilltop positions. Most generally, Eqs. 4 and 6 imply that soil mineral concentrations depend on the balance between the supply rate of primary minerals from bedrock and dust and the pace with which those primary minerals are chemically transformed into solutes and pedogenic phases. The former is primarily modulated by the erosion rate imposed by baselevel forcing and hillslope response, and the latter is determined by the relevant weathering rate constants (e.g., $K_{X,j}$) and soil particle residence times.

The rate constants for primary silicate mineral dissolution have been constrained under field and laboratory conditions and values vary with geologic context and climate (e.g., White and Brantley 2003). By contrast, rate constants relevant for modeling intermediate weathering pathways (such as alteration of PCMs to kaolinite and/or crystalline oxide phases) are lacking, although a limited number of chronosequence studies that track the formation of crystalline phases imply that the relevant timescales exceed 10^5 yr (Aniku and Singer 1990; Torn et al. 1997). Values of the soil production parameters P_0 and α have been shown to vary with climate and vegetation (Amundson et al. 2015).

Application to poorly crystalline mineral abundance

In order to assess how physical erosion rate, E, modulates the abundance of PCMs, we applied a simplified version of our generalized theoretical framework. First, we assume steady (or time-invariant) soil production, erosion, and weathering, which is relevant at the hillslope and catchment scale in most hilly and mountainous settings. Next, we neglect atmospheric deposition (i.e., $P_d = 0$) given that substantial dust contributions are typically associated with arid settings where PCM production is limited and thus less relevant for our approach. Third, following FK08, we non-dimensionalize Eqs. 4 and 6 using the relationships shown in Table 1. In particular, we define the non-dimensional physical erosion rate, $\widehat{E} = E/P_0$, which normalizes E with the peak soil production rate. In addition, we define $\widehat{K}_{X,j} = K_{X,j} t_p$, where $t_p = \rho_s / \left(P_0 \alpha\right)$, which represents the characteristic soil production time as defined by the soil production function parameters in Eq. 5. Given typical values of P_0 and α (Amundson et al. 2015), t_p is ~ 10^4 year. Although this timescale is closely related to the soil particle residence time, which is typically defined as the ratio of soil thickness to erosion rate (H/E), t_p does not vary with erosion rate and thus maintains a

Table 1 Relationships between dimensional and non-dimensional terms

Parameter	Non-dimensional version
Time, t	$\widehat{t} = (P_0 \alpha t)/\rho_s$
Physical erosion rate, E	$\widehat{E} = E/P_0$
Soil thickness, H	$\widehat{H} = \alpha H$
Effective reaction rate constant, $K_{X,j}$	$\widehat{K}_{X,j} = \left(\rho_s K_{X,j}\right)/\left(P_0 \alpha\right)$

constant value despite simulated variations in erosion rate. In this case, values of $\widehat{K}_{X,j}$ reflect the characteristic timescale of soil production relative to that of chemical reaction, which is similar to the Damkohler number often used in chemical weathering models subject to a swap of the numerator and denominator terms (Maher 2010).

Given these assumptions, we obtain the following dimensionless versions of Eqs. 4 and 6, where the ˆ symbol denotes a dimensionless term (note that C_{Xr} and C_{Xs} are dimensionless as defined here):

$$\frac{d\widehat{H}}{d\widehat{t}} = e^{-\widehat{H}} - \widehat{E} - \widehat{H}\sum_{j=1}^{n} C_{js}\widehat{K}_{j,sol} \tag{7}$$

$$\frac{dC_{Xs}}{d\widehat{t}} = \frac{e^{-\widehat{H}}}{\widehat{H}}\left(C_{Xr} - C_{Xs}\right) + \sum_{j=1}^{n} C_{js}\widehat{K}_{j,X} - C_{Xs}\left(\widehat{K}_{X,sol} + \sum_{j=1}^{n}\widehat{K}_{X,j} - \sum_{j=1}^{n} C_{js}\widehat{K}_{j,sol}\right) \tag{8}$$

Following Ferrier and West (2017), we use a nonlinear equation solver in Matlab (see supplemental materials) to simultaneously solve steady-state versions of Eqs. 7 and 8 (i.e., $dC_{Xs}/dt = 0, d\widehat{H}/dt = 0$) for all mineral phases. This framework enables us to generate predictions of C_{Xs} and $\widehat{H}$ for specified values of the dimensionless physical erosion rate ($\widehat{E}$), weathering rate constants ($\widehat{K}_{X,j}$), and bedrock (or substrate) mineral abundances (C_{Xr}). In applying this model, we focus on two stages of a weathering pathway that includes: (1) the creation of PCMs via weathering of primary minerals; and (2) their subsequent ripening and transformation into clays and crystalline oxide phases. In particular, we focus on the transformation of plagioclase into allophane (a common PCM on the aluminum weathering series) and its subsequent alteration into kaolinite and crystalline oxide phases, which are considered collectively for our simulations (Fig. 1). Specifically, we seek to determine whether our formulation generates soil allophane concentration ($C_{allo,s}$) erosion rate ($\widehat{E}$) relationships that yield a maximum value of $C_{allo,s}$, and thus an optimal erosion rate for facilitating MOC abundance.

For these calculations, we use a bedrock composition resembling a plagioclase-rich granite or immature sedimentary unit such as an arkosic sandstone with the following bedrock mineral fractions: quartz (0.25), plagioclase (0.4), potassium feldspar (0.2), and muscovite (0.15). In addition, we use the field-derived effective chemical solution rate constants listed in Table 2, which are chosen to be within an order of magnitude of values used in Ferrier and Kirchner (2008, supplemental Table C.1). The values used in FK08 account for grain roughness and surface area among other factors that govern the pace of mineral dissolution (Maher et al. 2009). Given our focus on weathering pathways that include the generation and subsequent ripening of allophane, we calculate how different values of $\widehat{K}_{plag,allo}$, which characterizes the rate at which plagioclase is transformed into allophane, and $\widehat{K}_{allo,kaol}$, which paces the ripening of allophane into kaolinite and crystalline phases, collectively influence how the concentration of allophane in soil ($C_{allo,s}$) varies with $\widehat{E}$. Put otherwise, we perform a sensitivity analysis to determine how different combinations of the plagioclase → allophane and allophane → kaolinite rate constants, which are poorly constrained by field studies, determine erosion rates that maximize allophane abundance in soil.

Table 2 Values of effective chemical reaction constants ($\widehat{K}_{X,j}$, $\widehat{K}_{j,X}$ and $\widehat{K}_{X,sol}$)

Parents	Daughters						
	Solutes	Quartz	Plagioclase	K-Feldspar	Muscovite	Kaolinite	Allophane
Quartz	1×10^{-4}	0	0	0	0	0	0
Plagioclase	1×10^{-1}	0	0	0	0	0	10^{-2} to 10^{0}
K-feldspar	1×10^{-2}	0	0	0	0	0	0
Muscovite	1×10^{0}	0	0	0	0	0	0
Kaolinite	1×10^{-3}	0	0	0	0	0	0
Allophane	1×10^{-2}	0	0	0	0	10^{-2} to 10^{0}	0

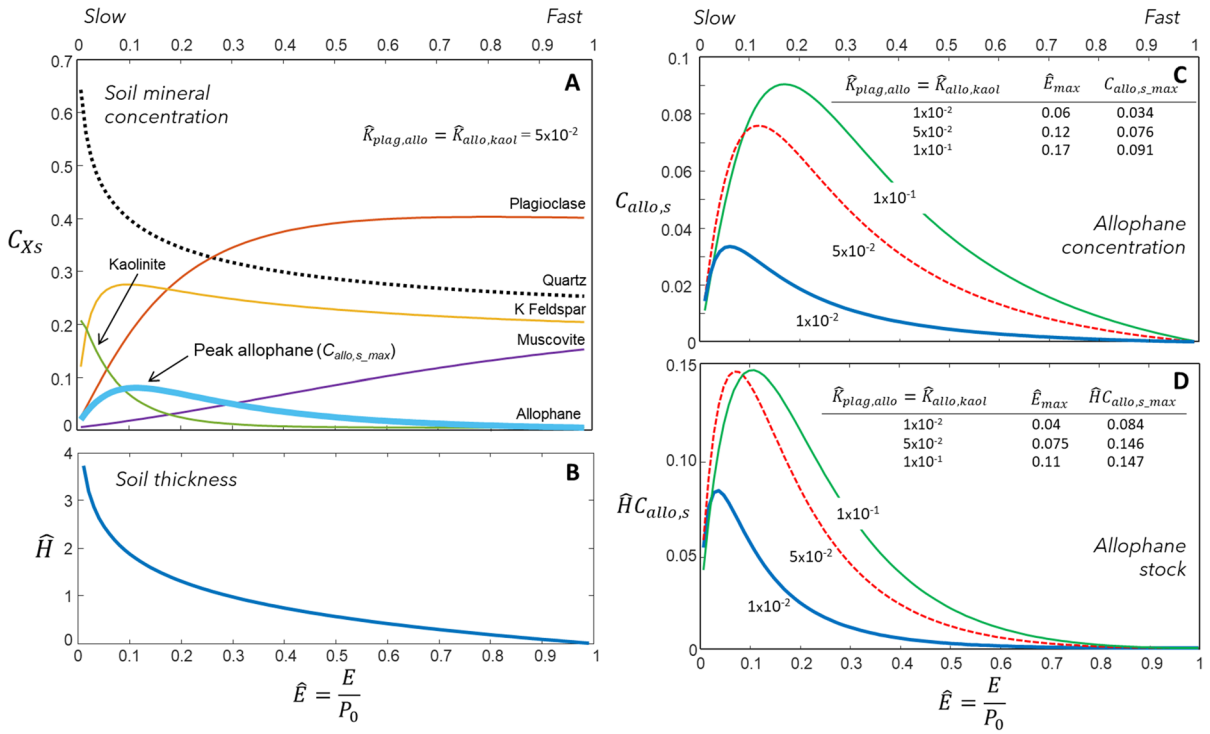

Fig. 2 **A** Dependence of mineral abundances on steady-state dimensionless erosion rate. **B** Variation of dimensionless soil thickness with dimensionless erosion rate. **C** The optimal erosion rate to maximize allophane abundance varies with the chemical reaction parameters for the transformations of plagioclase → allophane and allophane → clays and other crystalline phases. **D** Variation of the optimal erosion rate for peak allophane stocks, calculated as the product of dimensionless soil thickness and allophane abundance

Results

In order to generate steady-state $C_{allo,s}$-$\hat{E}$ relationships, we simultaneously solve steady-state versions of Eqs. 7 and 8 to simulate how the entire suite of mineral phases varies with $\hat{E}$. For a given value of $\hat{E}$, each simulation yields a suite of mineral concentrations that represents the composition of a steadily eroding ridge crest soil (Fig. 2A). For $\hat{K}_{plag,allo} = \hat{K}_{allo,kaol} = 5 \times 10^{-2}$, the soil mineral concentrations for values of $\hat{E}$ slightly below 1.0 are essentially equivalent to the bedrock concentrations listed above. These high $\hat{E}$ values correspond to erosion rates just below the peak soil production rate, P_0, which reflects a negligibly thin, minimally altered soil with values of $C_{allo,s}$ and $C_{kaol,s}$ equal to zero. With decreasing values of $\hat{E}$, our simulations show that individual mineral phases have different sensitivity to changes in $\hat{E}$, reflecting differential weathering as well as the onset of secondary mineral weathering pathways. For the simulation shown in Fig. 2A, these differential changes arise due to the rapid pace of muscovite and plagioclase dissolution relative to other minerals. In addition, with decreasing $\hat{E}$, the alteration of plagioclase into allophane results in increasing $C_{allo,s}$ values that peak at $0.1 < \hat{E} < 0.15$ (Fig. 2A). As $\hat{E} \rightarrow 0$, $C_{allo,s}$ values decline as long soil residence times allow for extensive transformation of allophane into kaolinite. At these near-zero values of $\hat{E}$, the modeled soil mineral composition becomes dominated by quartz and kaolinite as the extremely slow erosion rates result in near comprehensive dissolution of non-quartz primary minerals. Our simulations also provide steady-state values of soil thickness ($\hat{H}$) that declines rapidly with $\hat{E}$ (Fig. 2B), which is consistent with field observations (Heimsath et al. 1997).

To explore controls on the erosion rate that optimizes allophane abundance and constrain relevant values of the reaction rate constants for allophane and kaolinite, we generated $C_{allo,s}$-$\widehat{E}$ relationships for parameter combinations within the following bounds: $1 \times 10^{-2} \le \widehat{K}_{plag,allo} \le 1 \times 10^{0}$ and $1 \times 10^{-2} \le \widehat{K}_{allo,kaol} \le 1 \times 10^{0}$. For example, Fig. 2C shows $C_{allo,s}$-$\widehat{E}$ relationships for three parameter combinations where $\widehat{K}_{plag,allo} = \widehat{K}_{allo,kaol}$. For these simulations, as the value of $\widehat{K}_{allo,kaol}$ (and thus $\widehat{K}_{plag,allo}$) increases, the value of $\widehat{E}$ associated with peak allophane (termed $\widehat{E}_{max}$) also increases, along with the peak concentration of allophane (termed C_{allo,s_max}; Fig. 2C). In order to assess the optimal erosion rate for total allophane abundance, we estimated the allophane stock as the product of $\widehat{H}$ and $C_{allo,s}$ and modeled how the allophane stock varies with $\widehat{E}$ (Fig. 2D). According to this analysis, $\widehat{E}_{max}$ for allophane stocks is shifted to lower values owing to the nonlinearity of the $\widehat{H} - \widehat{E}$ relationship shown in Fig. 2B. For the remainder of our analysis, we focus on $\widehat{E}$ values that optimize $C_{allo,s}$ (rather than $\widehat{H}C_{allo,s}$), while retaining the understanding that consideration of allophane stocks slightly decreases values of $\widehat{E}_{max}$.

To determine how other combinations of $\widehat{K}_{allo,kaol}$ and $\widehat{K}_{plag,allo}$ impact the optimal erosion rate and peak allophane concentration, we modeled $C_{allo,s}$-$\widehat{E}$ relationships for various parameter combinations of $\widehat{K}_{plag,allo}$ and $\widehat{K}_{allo,kaol}$ and calculated $\widehat{E}_{max}$ (Fig. 3A) as well as C_{allo,s_max} (Fig. 3B). These simulations demonstrate that $\widehat{E}_{max}$ increases with $\widehat{K}_{allo,kaol}$ and/or $\widehat{K}_{plag,allo}$ with modeled values of $\widehat{E}_{max}$ varying from 0.08 to 0.5 for $\widehat{K}_{plag,allo} = \widehat{K}_{allo,kaol} = 1 \times 10^{-2}$ and $\widehat{K}_{plag,allo} = \widehat{K}_{allo,kaol} = 1 \times 10^{0}$, respectively (Fig. 3A). By contrast, Fig. 3B shows that C_{allo,s_max} is highest (0.35) for large values of $\widehat{K}_{plag,allo}$ and small values of $\widehat{K}_{allo,kaol}$, while low values of C_{allo,s_max} (< 0.05) are associated with low values of $\widehat{K}_{plag,allo}$ and high values of $\widehat{K}_{allo,kaol}$. The tradeoff between these two reaction constants reveals how the relative pace of allophane generation from plagioclase and subsequent alteration to kaolinite dictates the steady-state concentration of allophane in eroding soils. Because the concentration of poorly crystalline minerals seldom exceeds 4% (or 0.04) based on a meta-analysis of soil databases (Slesserav et al. 2022), our analysis implies that the parameters defined by the lower right corner of Fig. 3B (i.e., low values of $\widehat{K}_{plag,allo}$ and high values of $\widehat{K}_{allo,kaol}$) are most likely representative of natural landscapes. This region of the parameter space corresponds with $\widehat{E}$ values between 0.1 and 0.25.

Discussion

Our simulations reveal an optimal erosion rate that maximizes the concentration of PCMs: in this case allophane (Fig. 4A). When $\widehat{E}$ is high, erosion is rapid and/or soil is thin, which limits the production of PCMs. In essence, soil minerals move through the soil column too rapidly for significant weathering and PCM production to occur. By contrast, PCM ripening-limited conditions occur when $\widehat{E}$ is low, which corresponds to slow erosion with thick, intensely weathered soils, such that PCMs have largely been altered to clays and more crystalline pedogenic phases. At these low values of $\widehat{E}$, soil particle residence time is sufficiently long that PCM ripening has been pervasive, limiting the availability of PCMs available to form long-lived associations with SOC. Our theoretical findings are analogous to datasets derived from chronosequence studies in that PCM concentrations in soils increase with substrate age and attain a maximum value before decreasing with further increases in soil age. In Torn et al. (1997), the sweet spot for PCM concentrations and SOC abundance occurs on ~ 100-kya lava flows, whereas Garcia Arredondo et al. (2019), Hunter et al. (in press), and Lawrence et al. (2015) report soil PCM and SOC peaks at 90, 30, and 24 kya, respectively. While broadly consistent, the differences in these ages likely reflect parent material and climate variables that modulate mineral abundance and the pace of weathering processes, which are encapsulated in the $\widehat{K}_{X,j}$ terms. As elaborated by Mudd and Yoo (2010), these chronosequence studies, which are often used to quantify the mechanisms responsible for time-dependent changes in weathering rates (White and Brantley 2003), also do not account for the on-going influxes of primary minerals into the soil from underlying rock and/or dust, which resupply the soil column in erosional settings (Almond et al. 2007). Importantly, the erosion rate associated with peak PCM and

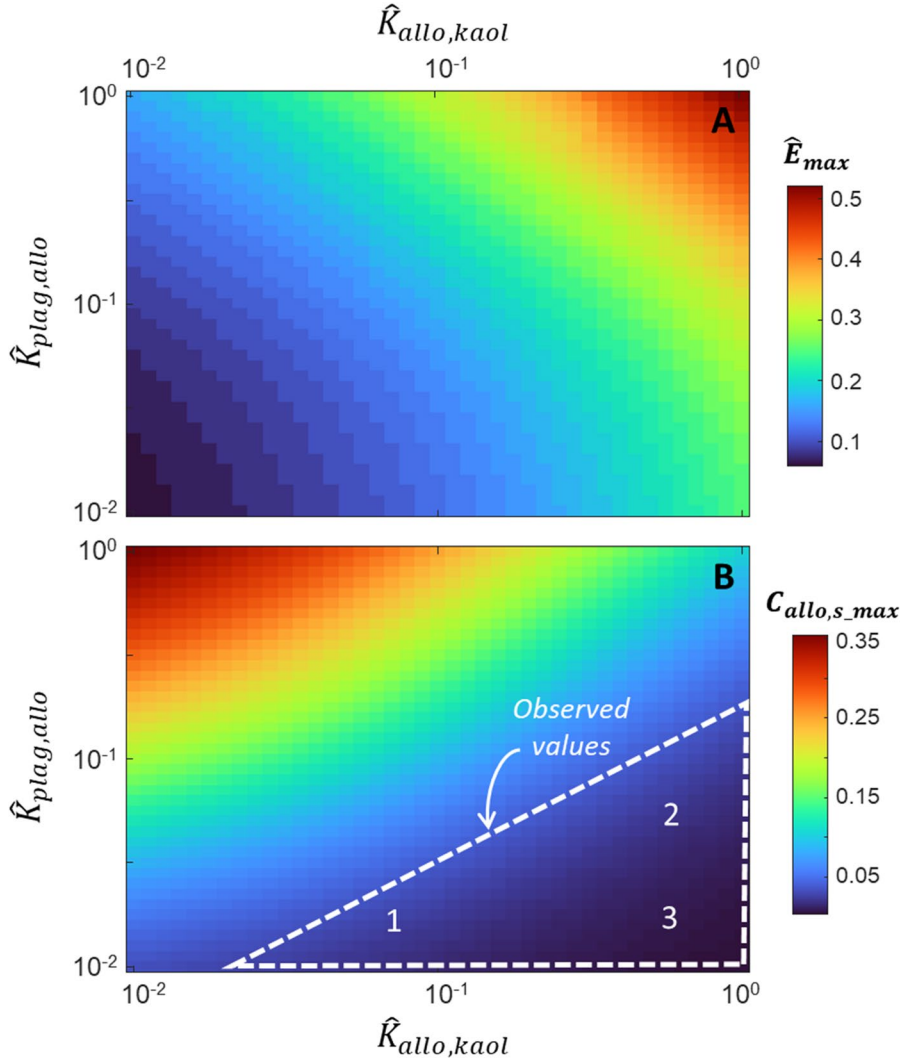

Fig. 3 Influence of reaction rate constants on the optimal erosion rate and peak allophane abundance. **A** Variation of optimal erosion rate ($\hat{E}_{max}$) for peak allophane abundance (see examples in Fig. 2C) with differing plagioclase → allophane and allophane → clays/crystalline phases rate constants. Note that increases in either rate constant results in higher values for the dimensionless erosion rate that maximizes allophane abundance. **B** Variation of peak allophane abundance (C_{allo,s_max}) with reaction rate constants, which shows that the relatively low PCM abundances (<4%) observed in soil geochemical databases (Slesserav et al. 2022) are associated with the slow transformation of plagioclase → allophane and relatively rapid transformation of allophane → clays/crystalline phases, which is reflected in the lower right corner of the plot and denoted by a dash white triangle. The numbers 1, 2, and 3 refer to the parameter combinations for simulations shown in Fig. 4A and represent the variability of weathering rate constants that are relevant to natural settings

SOC may be decoupled in some landscapes owing to biotic factors that modulate SOM inputs and microbial respiration, which can vary with aspect, slope, and local hydrologic context.

Here, we focus on modeling PCM abundances for predicting SOC sequestration potential across eroding landscapes, which could have meaningful implications for mapping and management. Nonetheless, our analysis is also relevant for assessing soil organic matter and other ecologically-important biogeochemical cycles like soil nitrogen and phosphorus, which also likely vary with the prevalence of PCMs (e.g., Eger et al. 2018). Furthermore, we acknowledge that PCMs are not the only means for generating

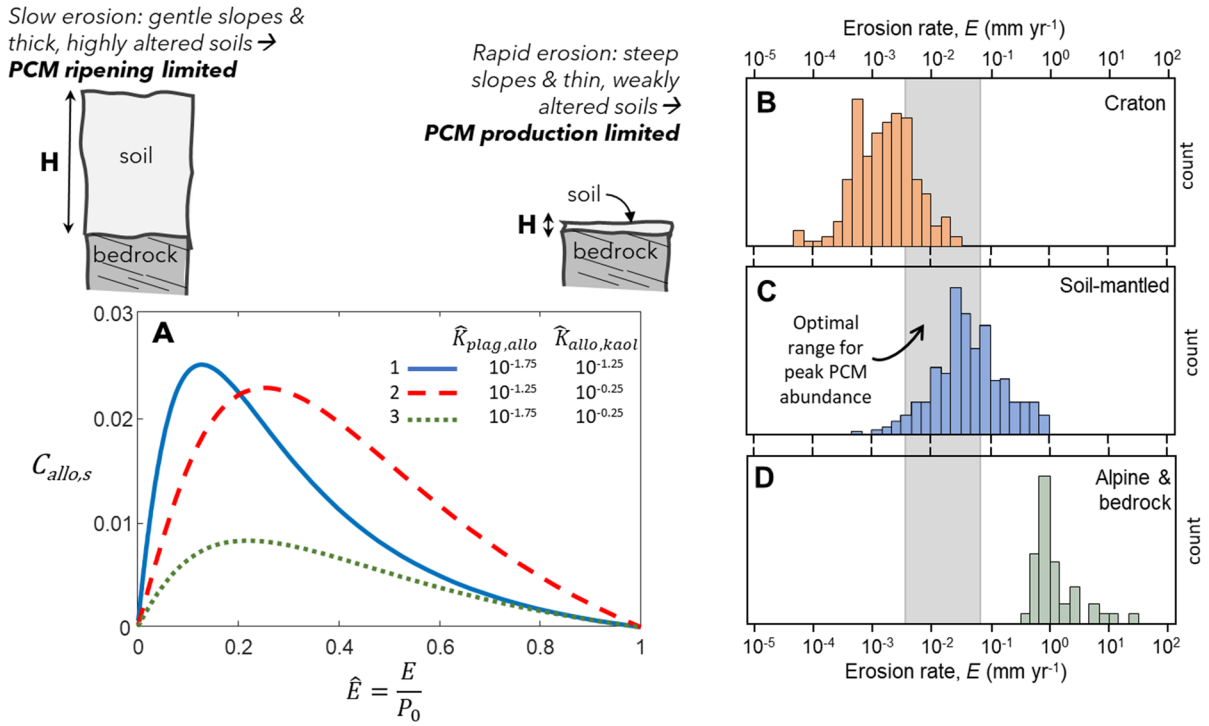

Fig. 4 **A** Erosion rate controls on soil PCM abundance (in this case allophane) for three simulations using parameter combinations that represent the highlighted region in Fig. 3B, which corresponds to values consistent with field observations. Whereas production limits PCM abundances in rapidly eroding landscapes, PCM alteration to clays and crystalline phases (via ripening) limits PCM abundance in slow-eroding landscapes. According to this analysis, optimal values of $\hat{E}$ for peak PCM abundance vary from 0.1 to 0.25. **B**–**D** Erosion rate compilation of Montgomery (2007), which implies that the faster eroding fraction of cratonic settings and slower eroding portion of soil-mantled settings likely harbor optimal PCM abundances, given the estimates of peak soil production rates from Amundson et al. (2015). Although these datasets estimate E and P_0 in dimensions of L T^{-1}, the values can be translated directly to our non-dimensional model framework

substantial MOC pools, given that certain clay minerals are also effective at forming organo-chemical associations—although often with decreased efficacy relative to PCMs. In many soils, the silt and clay fraction correlates with PCM abundance, although key differences have been documented (Rasmussen et al. 2018). In addition, our framework addresses PCM formation independent of the production of organic compounds available to sorb with PCM surfaces, which is requisite for SOC stabilization (Lehmann et al. 2020). Lastly, although our mass balance model assumes well-mixed soil and neglects significant alteration of the underlying substrate that would alter primary mineral abundance and PCM production, it could be adapted to accommodate substrate weathering that precedes soil production (i.e., weathering of saprolite), as well as incomplete and/or depth-dependent soil mixing.

The assumption of steady state erosion, soil thickness, and mineral composition employed here should not be confused with orogen- or even catchment-scale steady denudation (Willett and Brandon 2002), which are frequently violated as evidenced by the presence of knickpoints and other erosional gradients that result from baselevel changes and/or lithologic variations. Rather, our methodology assumes that local (i.e., pedon or solum) soil thickness and properties do not change substantially over timescales less than the soil particle residence time or characteristic soil production time. The steady-state assumption requires careful consideration in slow-eroding settings, which may record a longer history of perturbations related to climatic changes, as previous analyses

have demonstrated the key role of landscape age for predicting weathering intensity and soil mineralogy (Slessarev et al. 2019). As such, a transient analysis of our model predictions under different environmental forcings would be useful to assess the impact of interglacial-glacial fluctuations or other climate variations that determine model parameters (Ferrier and West 2017), particularly, P_0, α, and the rate constants $\widehat{K}_{plag,allo}$ and $\widehat{K}_{allo,kaol}$.

Given the strong coupling between erosion rate and tectonic setting, our findings imply that geologic factors may serve as a key bottom-up control on PCM abundance in soils. Montgomery (2007) parsed erosion rate data into cratons, soil-mantled hillslopes, and alpine or bedrock environments associated with rapid tectonic forcing and showed that erosion rates vary by $> 10^5$ amongst these settings (Fig. 4B–D). Importantly, erosion rates greater than 10^0 mm year^{-1} tend to occur in alpine or bedrock settings (Fig. 4D) with a patchy or non-existent soil mantle such that these landscapes have negligible potential for SOC storage and low PCM accumulation (Fig. 4A). In this regime, erosion rates equal or exceed peak soil production (P_0), corresponding with $\widehat{E} \geq 1$ in our framework. By contrast, highly-altered soils in slow-eroding cratonic settings with erosion rates lower than 10^{-3} mm year^{-1} may feature low PCM abundances owing to long soil residence times that facilitate substantial alteration of PCMs into less reactive crystalline phases (Fig. 4B; Doetterl et al. 2018). Our findings imply that maximum PCM abundances are likely associated with erosion rates that occur between these two end-member regimes, and more specifically, in the range of overlap between cratonic and soil-mantled settings (Fig. 4B, C). To generate this prediction, we used our results showing peak PCM concentrations for $0.1 < \widehat{E} < 0.25$ (Fig. 4A) and commonly observed P_0 estimates of 0.04 to 0.3 mm yr^{-1} (Amundson et al. 2015) to calculate optimal erosion rates according to $E = \widehat{E}P_0$. From this analysis, we determine that maximum PCM abundance occurs for erosion rates between 0.004 and 0.075 mm yr^{-1}, which is depicted by a vertical gray bar in Fig. 4B–D. Our analysis implies that while steep, rapidly eroding terrain that comprises a small fraction (5–10%) of Earth surface accounts for > 50% of global sediment flux (Larsen et al. 2014), gentle-to-moderate inclined terrain with slow-to-moderate erosion rates constitutes a substantial fraction of the Earth surface and harbors soils with abundant PCMs and elevated SOC sequestration potential. In addition, by combining our predicted PCM stocks with erosion rate data, our framework enables the estimation of erosional PCM export to fluvial systems and depositional zones although these calculations are beyond the scope of this contribution. Importantly, we note that PCM abundance is also attendant to climatic conditions favoring chemical weathering as well as parent materials rich in primary minerals like feldspars (Slessarev et al. 2022), such that our approach also requires consideration of climatic and lithologic constraints.

Our framework for weathering and PCM production across eroding landscapes offers a simplified perspective on coupled and highly nonlinear weathering processes that are often addressed with parameter-rich and computationally demanding reactive transport models (Li et al. 2017). These models, which have been successfully applied to chronosequences (Maher et al. 2009), can address the interdependencies of fluid flow, mineral supply, and weathering kinetics, and thus provide an opportunity to assess more sophisticated process linkages than incorporated in our framework. For example, our model does not explicitly account for production of kaolinite directly from plagioclase. Realistically, the rate of plagioclase weathering likely determines the partitioning into secondary phases such as allophane and kaolinite, although the solubility and kinetics of allophane strongly favor allophane production in most settings. A rigorous and mechanistic treatment of these and other relevant weathering pathway controls is possible (Zhu et al. 2010), although it lies beyond the scope of this contribution. Furthermore, our weathering paramterization is not equivalent to compilations of time-dependent rates that emerge from chronosequence field studies that do not account for the supply of fresh minerals via soil production (White and Brantley 2003). Despite these simplifications, our parsimonious approach reveals readily-accessible and testable insights that arise due to first-order process dependencies between erosion rates, soil weathering, PCM abundance, and SOC stabilization potential.

Datasets from soil-mantled settings that include soil mineralogy, SOC, and long-term erosion rate are limited, precluding our ability to rigorously test our framework. Notably, Wang et al. (2018, 2022) analyzed soils above and below a prominent channel

Table 3 Soil thickness, erosion rate, and Fe extraction data for Middle Fork Feather River soil-mantled hillslopes occurring above (POMD) and adjacent (BRC) to a major knickpoint as reported in Wang et al. (2018, 2022)

Site	Average soil thickness (m)	Average $Fe_{o\text{-}p}$ (mg gm^{-1})	$Fe_{o\text{-}p}$ inventory (kg m^{-2})	Topographic curvature (m^{-1})	Modeled local erosion rate (mm yr^{-1})
POMD	1.05	0.682	0.913	− 0.0046	0.023
BRC	0.5	0.454	0.331	− 0.017	0.087

$Fe_{o\text{-}p}$ is oxalate-extractable iron less pyrophosphate-extractable iron, a proxy for poorly crystalline minerals (PCM). Depth-averaged values of $Fe_{o\text{-}p}$ were generated by integrating profiles from several pits and dividing by the average soil thickness. $Fe_{o\text{-}p}$ stocks were calculated using soil bulk density values reported in Wang et al. (2018, 2022)

Topographic curvature was estimated using 1-m resolution airborne lidar data (opentopography.org) and the wavelet-based curvature algorithm of Struble and Roering (2021) evaluated at the location of sampling pits. The standard deviation of curvature values at each site is < 25%

Local erosion rates modeled using a linear transport model and soil transport coefficient, D, of 0.004 m^2 yr^{-1}, a typical value for forested settings (Perron 2017)

knickpoint in a tributary of the North Fork Feather River, California, to determine geomorphic controls on soil geochemistry, soil thickness, and SOC. The slow-eroding, above-knickpoint site (POMD) has thicker and more highly altered soils than the fast-eroding, below-knickpoint site (BRC). The authors used catchment-averaged erosion rates to define a nearly 10 × erosional gradient that distinguishes these two sites (POMD = 0.036 mm $year^{-1}$ and BRC = 0.25 mm $year^{-1}$, Wang et al. 2018), although we interpret the erosional gradient to be weaker owing to delayed hillslope adjustment at BRC (Hurst et al. 2012). Using local hilltop convexity calculated from wavelets and airborne lidar (Struble and Roering 2021) and a soil transport coefficient typical of similar forested settings (Perron 2017), we estimate that BRC erodes 3.5 × faster than POMD. Specifically, we calculate erosion rates of 0.087 and 0.023 mm $year^{-1}$ for BRC and POMD, respectively (Table 3). With respect to PCM abundance, the Wang et al. (2018, 2022) data show that BRC has less oxalate-extractable minus pyrophosphate-extractable iron ($Fe_{o\text{–}p}$), a commonly used proxy for PCMs, as well as a thinner soil mantle (Table 3). This observation is consistent with the production-limited regime of our conceptual model shown on the right side of Fig. 2B, C, which shows decreasing PCM abundance and thinner soils with increasing erosion rate. Although the $Fe_{o\text{-}p}$ abundance for POMD is only ~ 50% greater than that for BRC, the soil thickness difference between the two sites amplifies the contrast between these two site in estimates of the $Fe_{o\text{-}p}$ inventory as we observe a ~ 2.5 × difference in the $Fe_{o\text{-}p}$ stock between the two sites (Table 3), consistent with our predictions for PCM stocks shown in Fig. 2D. Given the small sample size (n = 2) and equivocal erosion rate estimates for BRC and POMD, these data do not allow for rigorous calibration or testing of our quantitative framework. Nonetheless, the trends in soil thickness and PCM abundance at these two proximal sites subject to differential erosion are consistent with the production-limited regime of our predictions (Fig. 4A). Additional field studies are needed to assess the potential utility of our modeling approach.

At the hillslope and catchment scale, analyses of soil thickness and SOC stocks using topography and geomorphic models have generated promising results (Patton et al. 2019), signaling the potential to leverage coupled process models for SOC prediction. Although our results are developed for a generic hilltop or ridge crest position, probabilistic soil transport simulations imply that soil residence time distributions are increasingly similar across hillslopes in the presence of vigorous soil mixing and absent transient adjustments in response to variations in channel incision (Furbish et al. 2018). From this perspective, our approach should have broad applicability to eroding landscapes in regions like the fertile Pacific Northwest, which contains substantial SOC stocks (Poggio et al. 2021). In western Oregon, for example, long-term erosion rate estimates generated from cosmogenic nuclides vary by orders of magnitude, reflecting the influence of variable rock uplift, knickpoint migration, and river network dynamics (Penserini et al. 2017). The resulting erosional gradients have generated systematic variations in channel steepness, hillslope angle, hilltop curvature, and soil thickness across a range of scales. Fortunately, these spatial patterns can be quantified in high resolution owing to publicly available airborne lidar data, which can be coupled with calibrated geomorphic transport models to predict erosion rate and soil thickness. In particular, erosion metrics based on hilltop convexity and

the steepness of debris flow channel networks have been tested and calibrated across the region (Pensserini et al. 2017; Roering et al. 2007). These models are capable of generating erosion rate and soil thickness predictions at the pedon, hillslope, and catchment scales (Hurst et al. 2012; Roering et al. 2007), facilitating our ability to address some of the scale-dependence challenges associated with building and applying SOC inventory models (O'Rourke et al. 2015).

Conclusion

Primary minerals that enter soils through bedrock weathering generate PCMs that associate with SOC exerting a strong geochemical control on terrestrial carbon abundance and persistence. Erosion rate and soil thickness are first-order controls on soil weathering pathways that modify the abundance of PCMs available to associate with SOC. We propose a soil weathering mass balance approach that reveals an optimal erosion rate for potential SOC storage, corresponding to the maximum PCM concentration in a steadily eroding landscape. In rapidly eroding terrain, our results show that PCM abundance is limited by two factors: rapid cycling of primary minerals and thin soils. By contrast, in slow-eroding settings, PCM abundance is limited by the ripening of PCMs into clays and other crystalline phases, which are less conducive to SOC association. In these slow-eroding scenarios, the slow supply of primary minerals from bedrock relative to the pace of weathering processes is a critical control on the abundance of PCMs in soil. Our results provide a framework for assessing erosional controls on weathering and SOC abundance across a range of scales, from plot and hillslope scales up to entire catchments and even tectonic regimes, independent of differences in parent material or biological drivers of SOC dynamics. When coupled with geologic and biological datasets, topographic erosion metrics, and high-resolution topography, our approach enables mapping of PCM abundance across regional scales, facilitating our ability to predict SOC storage potential and forecast SOC response to disturbances.

Acknowledgements The authors thank S. Sebestyen, E. Slessarev, and an anonymous reviewer for highly constructive comments that enhanced the manuscript, as well as M. Polizzotto, J. Watkins, and Q. Jin for insightful discussions. NSF award EAR-2136934 to J. Roering and L. Silva provided financial support.

Funding Funding was provided by National Science Foundation (Grant No. 2136934).

Data availability The authors declare that the data supporting the findings of this study are available through the code provided in the supplementary materials.

Declarations

Conflict of interest All of the authors declare that they have no conflicts of interest.

References

Almond P, Roering J, Hales TC (2007) Using soil residence time to delineate spatial and temporal patterns of transient landscape response. J Geophys Res. https://doi.org/10.1029/2006JF000568

Amundson R, Heimsath A, Owen J, Yoo K, Dietrich WE (2015) Hillslope soils and vegetation. Geomorphology 234:122–132. https://doi.org/10.1016/j.geomorph.2014.12.031

Aniku JRF, Singer MJ (1990) Pedogenic iron oxide trends in a marine terrace chronosequence. Soil Sci Soc Am J 54:147–152. https://doi.org/10.2136/sssaj1990.03615995005400010023x

Chorover J, Amistadi MK, Chadwick OA (2004) Surface charge evolution of mineral-organic complexes during pedogenesis in Hawaiian basalt. Geochim Cosmochim Acta 68:4859–4876. https://doi.org/10.1016/j.gca.2004.06.005

Doetterl S, Stevens A, Six J, Merckx R, Van Oost K, Casanova Pinto M, Casanova-Katny A, Muñoz C, Boudin M, Zagal Venegas E, Boeckx P (2015) Soil carbon storage controlled by interactions between geochemistry and climate. Nat Geosci 8:780–783. https://doi.org/10.1038/ngeo2516

Doetterl S, Berhe AA, Arnold C, Bodé S, Fiener P, Finke P, Fuchslueger L, Griepentrog M, Harden JW, Nadeu E, Schnecker J, Six J, Trumbore S, Van Oost K, Vogel C, Boeckx P (2018) Links among warming, carbon and microbial dynamics mediated by soil mineral weathering. Nat Geosci 11:589–593. https://doi.org/10.1038/s41561-018-0168-7

Eger A, Yoo K, Almond PC, Boitt G, Larsen IJ, Condron LM, Wang X, Mudd SM (2018) Does soil erosion rejuvenate the soil phosphorus inventory? Geoderma 332:45–59. https://doi.org/10.1016/j.geoderma.2018.06.021

Ferrier KL, Kirchner JW (2008) Effects of physical erosion on chemical denudation rates: a numerical modeling study of soil-mantled hillslopes. Earth Planet Sci Lett 272:591–599. https://doi.org/10.1016/j.epsl.2008.05.024

Ferrier KL, West N (2017) Responses of chemical erosion rates to transient perturbations in physical erosion rates,

and implications for relationships between chemical and physical erosion rates in regolith-mantled hillslopes. Earth Planet Sci Lett 474:447–456. https://doi.org/10.1016/j.epsl.2017.07.002

Furbish DJ, Roering JJ, Almond P, Doane TH (2018) Soil particle transport and mixing near a hillslope crest: 1. Particle ages and residence times. J Geophys Res Earth Surf 123:1052–1077. https://doi.org/10.1029/2017JF004315

Garcia Arredondo M, Lawrence CR, Schulz MS, Tfaily MM, Kukkadapu R, Jones ME, Boye K, Keiluweit M (2019) Root-driven weathering impacts on mineral-organic associations in deep soils over pedogenic time scales. Geochim Cosmochim Acta 263:68–84. https://doi.org/10.1016/j.gca.2019.07.030

Georgiou K, Malhotra A, Wieder WR, Ennis JH, Hartman MD, Sulman BN, Berhe AA, Grandy AS, Kyker-Snowman E, Lajtha K, Moore JAM, Pierson D, Jackson RB (2021) Divergent controls of soil organic carbon between observations and process-based models. Biogeochemistry. https://doi.org/10.1007/s10533-021-00819-2

Georgiou K, Jackson RB, Vindušková O, Abramoff RZ, Ahlström A, Feng W, Harden JW, Pellegrini AFA, Polley HW, Soong JL, Riley WJ, Torn MS (2022) Global stocks and capacity of mineral-associated soil organic carbon. Nat Commun 13:3797. https://doi.org/10.1038/s41467-022-31540-9

Grant KE, Galy VV, Haghipour N, Eglinton TI, Derry LA (2022) Persistence of old soil carbon under changing climate: The role of mineral-organic matter interactions. Chem Geol 587:120629. https://doi.org/10.1016/j.chemgeo.2021.120629

Hall SJ, Thompson A (2022) What do relationships between extractable metals and soil organic carbon concentrations mean? Soil Sci Soc Am J 86:195–208. https://doi.org/10.1002/saj2.20343

Heimsath AM, Dietrich WE, Nishiizumi K, Finkel RC (1997) The soil production function and landscape equilibrium. Nature 388:358–361. https://doi.org/10.1038/41056

Heimsath AM, DiBiase RA, Whipple KX (2012) Soil production limits and the transition to bedrock-dominated landscapes. Nat Geosci 5:210–214. https://doi.org/10.1038/ngeo1380

Hunter BD, Roering JJ, Almond PC, Chadwick O, Polizzotto ML, Silva LCR (in press) Pedogenic pathways and deep weathering controls on soil organic carbon in Pacific Northwest forest soils. Geoderma.

Hurst MD, Mudd SM, Walcott R, Attal M, Yoo K (2012) Using hilltop curvature to derive the spatial distribution of erosion rates: hilltop curvature predicts erosion rates. J Geophys Res Earth Surf. https://doi.org/10.1029/2011JF002057

Jobbágy EG, Jackson RB (2000) the vertical distribution of soil organic carbon and its relation to climate and vegetation. Ecol Appl 10:423–436. https://doi.org/10.1890/1051-0761(2000)010[0423:TVDOSO]2.0.CO;2

Kleber M, Bourg IC, Coward EK, Hansel CM, Myneni SCB, Nunan N (2021) Dynamic interactions at the mineral–organic matter interface. Nat Rev Earth Environ 2:402–421. https://doi.org/10.1038/s43017-021-00162-y

Kramer MG, Chadwick OA (2018) Climate-driven thresholds in reactive mineral retention of soil carbon at the global scale. Nat Clim Change 8:1104–1108. https://doi.org/10.1038/s41558-018-0341-4

Larsen IJ, Montgomery DR, Greenberg HM (2014) The contribution of mountains to global denudation. Geology 42:527–530. https://doi.org/10.1130/G35136.1

Lavallee JM, Soong JL, Cotrufo MF (2020) Conceptualizing soil organic matter into particulate and mineral-associated forms to address global change in the 21st century. Glob Change Biol 26:261–273. https://doi.org/10.1111/gcb.14859

Lawrence CR, Harden JW, Xu X, Schulz MS, Trumbore SE (2015) Long-term controls on soil organic carbon with depth and time: a case study from the Cowlitz River Chronosequence, WA USA. Geoderma 247–248:73–87. https://doi.org/10.1016/j.geoderma.2015.02.005

Lehmann J, Kleber M (2015) The contentious nature of soil organic matter. Nature 528:60–68. https://doi.org/10.1038/nature16069

Lehmann J, Hansel CM, Kaiser C, Kleber M, Maher K, Manzoni S, Nunan N, Reichstein M, Schimel JP, Torn MS, Wieder WR, Kögel-Knabner I (2020) Persistence of soil organic carbon caused by functional complexity. Nat Geosci 13:529–534. https://doi.org/10.1038/s41561-020-0612-3

Li L, Maher K, Navarre-Sitchler A, Druhan J, Meile C, Lawrence C, Moore J, Perdrial J, Sullivan P, Thompson A, Jin L, Bolton EW, Brantley SL, Dietrich WE, Mayer KU, Steefel CI, Valocchi A, Zachara J, Kocar B, Mcintosh J, Tutolo BM, Kumar M, Sonnenthal E, Bao C, Beisman J (2017) Expanding the role of reactive transport models in critical zone processes. Earth-Sci Rev 165:280–301. https://doi.org/10.1016/j.earscirev.2016.09.001

Maher K (2010) The dependence of chemical weathering rates on fluid residence time. Earth Planet Sci Lett 294:101–110. https://doi.org/10.1016/j.epsl.2010.03.010

Maher K, Steefel CI, White AF, Stonestrom DA (2009) The role of reaction affinity and secondary minerals in regulating chemical weathering rates at the Santa Cruz Soil Chronosequence, California. Geochim Cosmochim Acta 73:2804–2831. https://doi.org/10.1016/j.gca.2009.01.030

Masiello CA, Chadwick OA, Southon J, Torn MS, Harden JW (2004) Weathering controls on mechanisms of carbon storage in grassland soils. Glob Biogeochem Cycles. https://doi.org/10.1029/2004GB002219

Montgomery DR (2007) Soil erosion and agricultural sustainability. Proc Natl Acad Sci 104:13268–13272. https://doi.org/10.1073/pnas.0611508104

Mudd SM (2017) Detection of transience in eroding landscapes: detection of transience in eroding landscapes. Earth Surf Process Landf 42:24–41. https://doi.org/10.1002/esp.3923

Mudd SM, Yoo K (2010) Reservoir theory for studying the geochemical evolution of soils. J Geophys Res. https://doi.org/10.1029/2009JF001591

O'Rourke SM, Angers DA, Holden NM, McBratney AB (2015) Soil organic carbon across scales. Glob Change Biol 21:3561–3574. https://doi.org/10.1111/gcb.12959

Patton NR, Lohse KA, Seyfried MS, Godsey SE, Parsons SB (2019) Topographic controls of soil organic carbon on

soil-mantled landscapes. Sci Rep 9:1–15. https://doi.org/10.1038/s41598-019-42556-5

Penserini BD, Roering JJ, Streig A (2017) A morphologic proxy for debris flow erosion with application to the earthquake deformation cycle, Cascadia Subduction Zone, USA. Geomorphology 282:150–161. https://doi.org/10.1016/j.geomorph.2017.01.018

Perron JT (2017) Climate and the pace of erosional landscape evolution. Annu Rev Earth Planet Sci 45:561–591. https://doi.org/10.1146/annurev-earth-060614-105405

Poggio L, de Sousa LM, Batjes NH, Heuvelink GBM, Kempen B, Ribeiro E, Rossiter D (2021) SoilGrids 2.0: producing soil information for the globe with quantified spatial uncertainty. Soil 7:217–240. https://doi.org/10.5194/soil-7-217-2021

Rasmussen C, Heckman K, Wieder WR, Keiluweit M, Lawrence CR, Berhe AA, Blankinship JC, Crow SE, Druhan JL, Hicks Pries CE, Marin-Spiotta E, Plante AF, Schädel C, Schimel JP, Sierra CA, Thompson A, Wagai R (2018) Beyond clay: towards an improved set of variables for predicting soil organic matter content. Biogeochemistry 137:297–306. https://doi.org/10.1007/s10533-018-0424-3

Roering JJ, Perron JT, Kirchner JW (2007) Functional relationships between denudation and hillslope form and relief. Earth Planet Sci Lett 264:245–258. https://doi.org/10.1016/j.epsl.2007.09.035

Schmidt MWI, Torn MS, Abiven S, Dittmar T, Guggenberger G, Janssens IA, Kleber M, Kögel-Knabner I, Lehmann J, Manning DAC, Nannipieri P, Rasse DP, Weiner S, Trumbore SE (2011) Persistence of soil organic matter as an ecosystem property. Nature 478:49–56. https://doi.org/10.1038/nature10386

Slessarev EW, Feng X, Bingham NL, Chadwick OA (2019) Landscape age as a major control on the geography of soil weathering. Glob Biogeochem Cycles 33:1513–1531. https://doi.org/10.1029/2019GB006266

Slessarev EW, Chadwick OA, Sokol NW, Nuccio EE, Pett-Ridge J (2022) Rock weathering controls the potential for soil carbon storage at a continental scale. Biogeochemistry 157:1–13. https://doi.org/10.1007/s10533-021-00859-8

Struble WT, Roering JJ (2021) Hilltop curvature as a proxy for erosion rate: wavelets enable rapid computation and reveal systematic underestimation. Earth Surf Dyn 9:1279–1300. https://doi.org/10.5194/esurf-9-1279-2021

Torn MS, Trumbore SE, Chadwick OA, Vitousek PM, Hendricks DM (1997) Mineral control of soil organic carbon storage and turnover. Nature 389:170–173. https://doi.org/10.1038/38260

von Fromm SF, Hoyt AM, Lange M, Acquah GE, Aynekulu E, Berhe AA, Haefele SM, McGrath SP, Shepherd KD, Sila AM, Six J, Towett EK, Trumbore SE, Vågen T-G, Weullow E, Winowiecki LA, Doetterl S (2021) Continental-scale controls on soil organic carbon across sub-Saharan Africa. Soil 7:305–332. https://doi.org/10.5194/soil-7-305-2021

Wang X, Yoo K, Mudd SM, Weinman B, Gutknecht J, Gabet EJ (2018) Storage and export of soil carbon and mineral surface area along an erosional gradient in the Sierra Nevada, California. Geoderma 321:151–163. https://doi.org/10.1016/j.geoderma.2018.02.008

Wang X, Wackett AA, Toner BM, Yoo K (2022) Consistent mineral-associated organic carbon chemistry with variable erosion rates in a mountainous landscape. Geoderma 405:115448. https://doi.org/10.1016/j.geoderma.2021.115448

White AF, Brantley SL (2003) The effect of time on the weathering of silicate minerals: why do weathering rates differ in the laboratory and field? Chem Geol 202:479–506. https://doi.org/10.1016/j.chemgeo.2003.03.001

Willett SD, Brandon MT (2002) On steady states in mountain belts. Geology 30:175. https://doi.org/10.1130/0091-7613(2002)030%3c0175:OSSIMB%3e2.0.CO;2

Zhu C, Lu P, Zheng Z, Ganor J (2010) Coupled alkali feldspar dissolution and secondary mineral precipitation in batch systems: 4. Numerical modeling of kinetic reaction paths. Geochim Cosmochim Acta 74:3963–3983. https://doi.org/10.1016/j.gca.2010.04.012